

Bi-fidelity sparse-grid interpolation driven by a local-error estimator

Matteo Rosellini¹, Filippo Fruzza¹, Alessandro Mariotti¹, Maria Vittoria Salvetti¹, and Lorenzo Tamellini²

¹Dipartimento di Ingegneria Civile e Industriale, University of Pisa, Italy

²CNR-IMATI, National Research Council - Institute for Applied Mathematics and Information Technologies, Pavia, Italy

March 10, 2026

Abstract Sparse grids based on Lagrange polynomials have become one of the staple methods for approximating functions that are high-dimensional and expensive to evaluate, in the context e.g. of PDE-based parametric design exploration. They are however known to be inefficient for problems requiring local refinement, such as when the target function exhibits localized features or sharp gradients. While locally-refined sparse grids based e.g. on piecewise linear polynomials are a well-established alternative to circumvent this problem, in this work we present a strategy for improving the local efficiency of Lagrangian sparse grids. We do so by building the sparse grid approximation incrementally and evaluating the function only at collocation points at which a suitable (and crucially, zero-cost) error indicator suggest that incorporating the function evaluation would significantly change the landscape of the approximation. The remaining collocation points are instead assigned values predicted by the already available sparse grid, i.e., following a bifidelity approach that reduces costs while preserving accuracy. The effectiveness of this methodology is demonstrated on several benchmark analytical functions and an engineering application concerning flashback phenomena in hydrogen-fueled perforated burners.

Keywords PDE-based parametric design; bifidelity surrogate models; sparse grids surrogate models; local-error indicators; complex flow applications; hydrogen-fueled perforated burners; flashback phenomena.

1 Introduction

The analysis and design of complex engineering systems frequently rely on high-fidelity computational models - typically, a set of partial differential equations (PDEs) to be solved. While these models provide accurate predictions, their significant computational cost often makes their use impractical in scenarios that require repeated evaluating them for different configurations, such as uncertainty quantification, parametric design exploration, and optimization. To overcome this limitation, surrogate modeling, i.e., deriving approximations of the original high-fidelity model, that can be evaluated at a significantly reduced computational cost, has emerged as a powerful and widely adopted strategy.

In this work, we focus on parametric design exploration for parametric PDEs, i.e., our goal is to assess the variability of the solution of a PDE (or of a quantity of interest derived from it) due to the fact that some (possibly many) parameters of the PDE can vary within design ranges. In this context, one typically needs to evaluate the high-fidelity model for several different values of the parameters, which is feasible with acceptable computational costs only if good surrogate models are available.

Among the many surrogate modeling techniques available in the literature [1], we focus here on sparse grids, which are a well-established technique [2, 3, 4]. This technique is a collocation approach, i.e., it recasts the problem of building a surrogate model as an interpolation problem over the parametric domain: the PDE solver is seen as a multi-variate function from the space of parameters to the space of the PDE solutions, which gets evaluated for a set for suitably-chosen values of the parameters; the corresponding

results are then interpolated by polynomials to obtain the surrogate model. This method is known to be moderately resilient to the so-called *curse of dimensionality* [5], i.e., they can be successfully applied in scenarios with up to say a few tens of parameters.

In particular, in this work we consider sparse grids that employ Lagrange polynomials as basis functions for the interpolation procedure. This strategy is effective for a large class of applications, thanks to the spectral accuracy of the Lagrange polynomials if appropriate collocation points are chosen [6, 7, 8, 9], but is unsuitable for problems that require local adaptivity, i.e., for situations in which the function to be approximated is characterized by localized features or sharp gradients. Versions of sparse grids that employ low-degree piecewise polynomials as basis functions and support local adaptivity, i.e. in which collocation points are concentrated near the above-mentioned features and gradients, are known in literature [10, 11, 12, 13, 14, 15]. However, the high-order convergence and continuity of Lagrange polynomials is lost, and the resulting algorithm could end up being nonetheless expensive, especially since these algorithms are typically *a-posteriori* and therefore a certain number of function evaluations is “wasted” on exploring regions of the parameter space that are ultimately not marked for refinement.

In this work, we thus explore a different and somehow “dual” approach: rather than striving to optimize the distribution of the collocation points, we aim at reducing the cost of evaluating the function over a “standard” set of collocation points, by building the sparse grid incrementally and leveraging on intermediate sparse grids both as zero-cost surrogates and zero-cost error indicators (contrary to the expensive error indicators of the classical *a-posteriori* local adaptivity). More specifically, we interpret the construction of a *target* sparse grid as a refinement step of a *baseline* sparse grid, which in turn can be seen as a refinement step of a *coarse* sparse grid; we further assume nestedness of the three sparse grids. Upon constructing the baseline sparse grids, the coarse sparse grid is thus also available, and their difference can be used as a zero-cost local error indicator, that we evaluate for all the collocation points where we still need to evaluate the function to build the target sparse grid (*candidate points*). The candidates are ranked by this metric, to select the points for which obtaining the actual function evaluation is expected to be most impactful in changing the landscape of the approximation, subject to a computational budget or a specific error threshold. The final sparse grid is constructed evaluating the function only at the selected points, whereas the remaining collocation points are instead assigned values predicted by the already available sparse grid. This bifidelity strategy, although admittedly quite simple, dramatically reduces the number of expensive function evaluations and achieves remarkable results, yielding a final surrogate model that closely approximates the accuracy of a fully-resolved, target sparse grid at a fraction of the computational cost.

The proposed methodology bears some similarity with other contributions in the literature of surrogate modeling for parametric PDEs. For instance, [16, 17] discuss a bi-fidelity low-rank approach to surrogate modeling construction, in which the two different fidelities can be either different discretizations of the same PDE, or different equations for the same physical phenomenon, whereas in our methodology the low-fidelity is the baseline sparse grid and the high-fidelity is the full function evaluation; [18, 19] consider so-called delayed-acceptance algorithms in which a cheap surrogate is evaluated prior to deciding whether the expensive function should be evaluated at the proposal sample of a Markov Chain Monte Carlo sampler; [20, 21, 22] propose to construct a surrogate model for the error of a reduced basis (similarly to our zero-cost error indicator), that can be incorporated in the construction of the reduced basis to improve its accuracy; finally, [23] shows how a sparse grid can be used as a control variate for a Monte Carlo sampling approach. To the best of our knowledge, this is however the first work in which a bi-fidelity/error indicator approach is used purely in the context of a sparse grid construction. Moreover, compared to [16, 17, 20, 21, 22] our error indicator is truly zero-cost, and can be implemented with very minimal overhead on pre-existing software; in particular, we have used to this end a Python code that draws inspiration from the Sparse Grids Matlab Kit [24] and that we make publicly available (see Data Availability Statement at the end of this manuscript for details).

The structure of this work is as follows. In Section 2, we present the theoretical foundations of our sparse grids surrogate model, specifically describing the proposed error indicator in Section 2.2 and designing the final bifidelity surrogate model in Section 2.3. Section 3 is devoted to assessing the performance of the proposed framework: we begin by testing it on a set of analytical benchmark functions commonly used in uncertainty quantification, including the Sobol G-function (Section 3.1.1), the Ishigami function (Section 3.1.2), and a highly oscillatory function (Section 3.1.3). Finally, in Section 3.2, we demonstrate the applicability of our method to a real-world scenario involving hydrogen-fueled perforated burners.

2 Methodology

2.1 Sparse grid interpolation: background and notation

We begin by recalling the essential concepts and notation of sparse grid interpolation upon which our method is built; here, we follow closely the setup of [24], to which we refer readers interested in a more thorough discussion and further bibliographic references.

We consider the problem of approximating a scalar quantity of interest $f(\mathbf{x}) : \Gamma \subset \mathbb{R}^d \rightarrow \mathbb{R}$, where $\mathbf{x} = (x_1, \dots, x_d)$ denotes a vector of d input parameters taking values in $\Gamma = \Gamma_1 \times \dots \times \Gamma_d \subset \mathbb{R}^d$, each possibly unbounded and characterized by a probability density function (PDF) $\rho_n : \Gamma_n \rightarrow \mathbb{R}^+$, $n = 1, \dots, d$. The specific choice of these PDFs encodes a-priori knowledge/preferences (or uncertainty) on the values of the parameters, and it could be, e.g., constant, Gaussian or exponential depending on the specific application, or it may be even available only implicitly as samples obtained from an experiment or a Bayesian computation [25]. In this work we assume that $\Gamma = \Gamma_1 \times \dots \times \Gamma_d$ is a bounded hyper-rectangular domain and that there are no preferred values for the parameters, i.e., we consider constant PDFs $\rho_n = \frac{1}{|\Gamma_n|}$. We further assume that the parameters are independent, such that their joint PDF reads $\rho(\mathbf{x}) = \prod_{n=1}^d \rho_n(x_n)$.

In this setting, sparse grids provide an efficient collocation-based strategy to construct an interpolant of f . The construction begins with a family of one-dimensional points for each parameter. For $n = 1, \dots, d$ and univariate level $i \in \mathbb{N}_+$, we introduce a set of collocation points

$$\mathcal{X}_i^{(n)} = \left\{ x_{i,j}^{(n)} \right\}_{j=1}^{m(i)},$$

where $m : \mathbb{N}_+ \rightarrow \mathbb{N}_+$ is a function that prescribes the number of points at each level. In practice, the points for each parameter x_n are chosen according to ρ_n to improve sampling efficiency and accuracy. Specifically, in this work we employ specifically Clenshaw–Curtis points, which are a classical choice whenever the parameters have a constant PDF. Clenshaw–Curtis points are defined on a reference interval $[-1, 1]$ as

$$x_{i,j}^{(n)} = \cos\left(\frac{(j-1)\pi}{m(i)-1}\right), \quad j = 1, \dots, m(i),$$

and mapped to Γ_n via an affine transformation. If $m(i)$ is chosen as $m(i) = 2^{i-1} + 1$, these points are nested, i.e. $\mathcal{X}_i^{(n)} \subset \mathcal{X}_{i+1}^{(n)}$, allowing collocation points from coarser levels to be systematically reused at finer levels. This nested structure is a key ingredient of the bifidelity procedure proposed in this work.

Given a multi-index $\mathbf{i} = (i_1, \dots, i_d) \in \mathbb{N}_+^d$, a tensor-product grid then is defined as the Cartesian product

$$\mathcal{X}_{\mathbf{i}} = \bigotimes_{n=1}^d \mathcal{X}_{i_n}^{(n)}.$$

On this grid, a tensor-product interpolant can be constructed via standard multivariate Lagrange interpolation. Denoting the associated operator by $\mathcal{U}_{\mathbf{i}}$, the approximation is given by

$$\mathcal{U}_{\mathbf{i}}[f](\mathbf{x}) = \sum_{\mathbf{x}_{i,j} \in \mathcal{X}_{\mathbf{i}}} f(\mathbf{x}_{i,j}) \mathcal{L}_{\mathbf{i},j}(\mathbf{x}),$$

where $\mathcal{L}_{\mathbf{i},j}$ are the standard tensor-product multivariate Lagrange polynomials, i.e., $\mathcal{L}_{\mathbf{i},j}(\mathbf{x}_{i,k}) = \delta_{j,k}$. While tensor-product interpolation provides high accuracy, their size grows exponentially with d . Sparse grids mitigate this issue by combining a carefully selected set of anisotropic tensor interpolants through the so-called *combination technique*. In its standard form, given an integer value w (*sparse-grid level*) the sparse grid operator is expressed as a weighted sum

$$\mathcal{A}_w[f](\mathbf{x}) = \sum_{\mathbf{i} \in \mathcal{I}_w} c_{\mathbf{i}} \mathcal{U}_{\mathbf{i}}[f](\mathbf{x}),$$

where the integer coefficients $c_{\mathbf{i}}$ are given by the combination technique formula

$$c_{\mathbf{i}} = \sum_{\substack{\boldsymbol{\delta} \in \{0,1\}^d \\ \mathbf{i} + \boldsymbol{\delta} \in \mathcal{I}_w}} (-1)^{\|\boldsymbol{\delta}\|_1},$$

and $\mathcal{I}_w = \{\mathbf{i} \in \mathbb{N}_+^d : |\mathbf{i}|_1 \leq w + d - 1\}$. The latter is a classical choice for \mathcal{I}_w , but other choices are possible, see e.g. [24]. The associated sparse grid set is defined as the union of all tensor grids entering the combination:

$$\mathcal{X}_w = \bigcup_{\mathbf{i} \in \mathcal{I}_w} \mathcal{X}_{\mathbf{i}}.$$

Note that if nested univariate points are used, $\mathcal{X}_{\mathbf{i}}^n \subset \mathcal{X}_{\mathbf{i}+1}^n$, the sparse grids are also nested, $\mathcal{X}_{w-1} \subset \mathcal{X}_w$.

2.2 A zero-cost error indicator

As already discussed in the introduction, in this work we focus on functions f that have localized features or sharp gradients, for which sparse grids based on Lagrangian polynomials can be expected to behave poorly, since their convergence estimates depend on the norms of the derivatives of f , see e.g. [6, 7]. However, we do not want to circumvent this issue by resorting to locally adaptive sparse grids, which can be expensive due to the *a-posteriori* algorithmic nature, i.e., the fact that refinement typically happens only after having spent a significant computational cost to evaluate f over a carefully-defined set of candidate points. Instead, we propose to consider a “simple” and fairly large set of candidates, naturally inspired by the nested structure of the sparse grid construction, and to decide next where the function f should be evaluated, based on a zero-cost local error indicator that exclusively relies on the evaluations of f that are already available.

More specifically, let us assume that our final goal is to obtain a sparse grid approximation $\mathcal{A}_{w+1}[f]$, that we call *target* sparse grid, for some fixed w . Due to the nestedness of the Clenshaw–Curtis points, this grid can be computed as a refinement of a *baseline* sparse grid approximation $\mathcal{A}_w[f]$, that we assume to have at disposal. Moreover, again by nestedness, this implies that we also have at disposal a *coarse* sparse grid approximation $\mathcal{A}_{w-1}[f]$. We can then define a pointwise discrepancy, Δ , as the absolute difference between these two surrogates:

$$\Delta(\mathbf{x}) = |\mathcal{A}_w[f](\mathbf{x}) - \mathcal{A}_{w-1}[f](\mathbf{x})|$$

This discrepancy is available at no further computational cost, i.e., it does not require any further evaluation of f , and can be evaluated for every point of the parametric space Γ . In particular, it can be evaluated for each point in

$$\mathcal{X}_{\text{cand}} = \mathcal{X}_{w+1} \setminus \mathcal{X}_w,$$

i.e., the set of points that are required to build the target sparse grid upon having built the baseline one. A large discrepancy at a point of $\mathcal{X}_{\text{cand}}$ indicates that the coarse sparse grid is locally under-resolved, and therefore that additional evaluations of f in the same region are likely to be still beneficial. The final local error indicator, η , is actually formulated as a hybrid relative-absolute error, to avoid instabilities when the predicted value $\mathcal{A}_w[f]$ is close to zero. The error indicator is thus defined as:

$$\eta(\mathbf{x}) = \begin{cases} \frac{|\Delta(\mathbf{x})|}{|\mathcal{A}_w[f](\mathbf{x})|} & \text{if } |\mathcal{A}_w[f](\mathbf{x})| > \epsilon \\ |\Delta(\mathbf{x})| & \text{if } |\mathcal{A}_w[f](\mathbf{x})| \leq \epsilon \end{cases} \quad (1)$$

where ϵ is a small numerical tolerance (e.g., 10^{-12}). Once the indicator η has been computed for each candidate point in $\mathcal{X}_{\text{cand}}$, these points are sorted in descending order according to their indicator values. To determine at which points f should be evaluated, several selection strategies can be considered. In this work, we focus on three representative approaches:

1. Fixed budget: The top B candidates are selected, where B is a predefined computational budget.
2. Relative threshold: All candidates whose indicator value exceeds a fraction τ of the maximum observed indicator, η_{max} , are selected. The set is thus defined as

$$\mathcal{X}_{\text{sel}} = \{\mathbf{x} \in \mathcal{X}_{\text{cand}} \mid \eta(\mathbf{x}) \geq \tau \cdot \eta_{\text{max}}\}. \quad (2)$$

3. Elbow identification: This strategy employs a geometric heuristic to determine the optimal cutoff point in the sorted indicator curve. Let $P = \{(i, \eta_{(i)})\}_{i=1}^N$ be the set of points representing the sorted candidate indices and their corresponding indicator values. We define a straight line connecting the first point $(1, \eta_{\text{max}})$ and the last point (N, η_{min}) . For each point $p_i \in P$, we calculate the

perpendicular distance $d(p_i, \ell)$ to this line. The *elbow* is identified as the point p_k that maximizes this distance:

$$k = \underset{i}{\operatorname{argmax}} d(p_i, \ell)$$

The number of selected points is set to k . This approach provides a balance between accuracy and computational cost without requiring pre-tuned hyperparameters.

2.3 Design of the final surrogate model

Once the set of points marked for evaluation \mathcal{X}_{sel} is available, we can construct the final surrogate model. Crucially, this is *not* the target sparse grid $\mathcal{A}_{w+1}[f]$, but rather a hybrid/bifidelity surrogate model $\mathcal{B}[f] \approx \mathcal{A}_{w+1}$, in which the points in $\mathcal{X}_{\text{cand}} \setminus \mathcal{X}_{\text{sel}}$ will be assigned the value of $\mathcal{A}_w[f]$ rather than f . Equivalently, $\mathcal{B}[f]$ can be seen as the sparse grid approximation of a generic continuous function g whose value in the collocation points \mathcal{X}_{w+1} is defined as follows:

$$\mathcal{B}[f] = \mathcal{A}_{w+1}[g], \quad g(\mathbf{x}_k) = \begin{cases} f(\mathbf{x}_k) & \text{if } \mathbf{x}_k \in \mathcal{X}_{\text{sel}} \cup \mathcal{X}_w \\ \mathcal{A}_w[f](\mathbf{x}_k) & \text{if } \mathbf{x}_k \in \mathcal{X}_{\text{cand}} \setminus \mathcal{X}_{\text{sel}} \end{cases}. \quad (3)$$

We conclude this section by remarking that it is possible to rewrite $\mathcal{B}[f]$ to highlight its *incremental* nature by rewriting $g = \mathcal{A}_w[f] + \delta$, with

$$\delta(\mathbf{x}_k) = \begin{cases} f(\mathbf{x}_k) - \mathcal{A}_w[f](\mathbf{x}_k) & \text{if } \mathbf{x}_k \in \mathcal{X}_{\text{sel}} \cup \mathcal{X}_w \\ 0 & \text{if } \mathbf{x}_k \in \mathcal{X}_{\text{cand}} \setminus \mathcal{X}_{\text{sel}} \end{cases}.$$

and then noting that

$$\mathcal{B}[f] = \mathcal{A}_{w+1}[g] = \mathcal{A}_{w+1}[\mathcal{A}_w[f] + \delta] = \mathcal{A}_w[f] + \mathcal{A}_{w+1}[\delta],$$

where in the last equality we have used the linearity of the interpolation operators and the fact that $\mathcal{A}_w[f]$ is a polynomial that can be interpolated exactly by \mathcal{A}_{w+1} due to the nestedness of the corresponding grids. The rightmost expression shows how $\mathcal{B}[f]$ can be obtained by adding the interpolant of a suitable correction/increment term to the baseline sparse grid $\mathcal{A}_w[f]$, in the spirit of [20, 21].

3 Results

To validate the performance of our approach, we first apply it to some analytical functions that are notoriously challenging for surrogate modeling (Section 3.1), and then move to a practical engineering case study (Section 3.2). For all these tests, we consider a relatively coarse baseline and target sparse grid ($w = 2$ and $w = 3$, respectively): this setting reflects realistic engineering constraints, where the high computational cost of simulations allows only for very few full model evaluations; this is indeed exemplified in Section 3.2. Note that in this sense the dimension-adaptive sparse grids [26, 24] are not a viable option to derive a baseline sparse grid, since they are also a-posteriori algorithms that invests a non-negligible cost at the beginning of the computation to assess what parameters are most influential and hence worth refining.

3.1 Validation on analytical benchmark functions

The chosen benchmark functions, Sobol’s G-function [27], Ishigami function [28] and an oscillatory function, test the algorithm’s ability to handle strong non-linearities, parameter interactions, and non-smooth features [29].

3.1.1 The Sobol G-function

The Sobol G-function [27] is a scalable, high-dimensional benchmark characterized by discontinuities in its derivatives. For our analysis, we used its $d = 4$ -dimensional version, defined as:

$$f(\mathbf{x}) = \prod_{i=1}^d \frac{|4x_i - 2| + a_i}{1 + a_i}$$

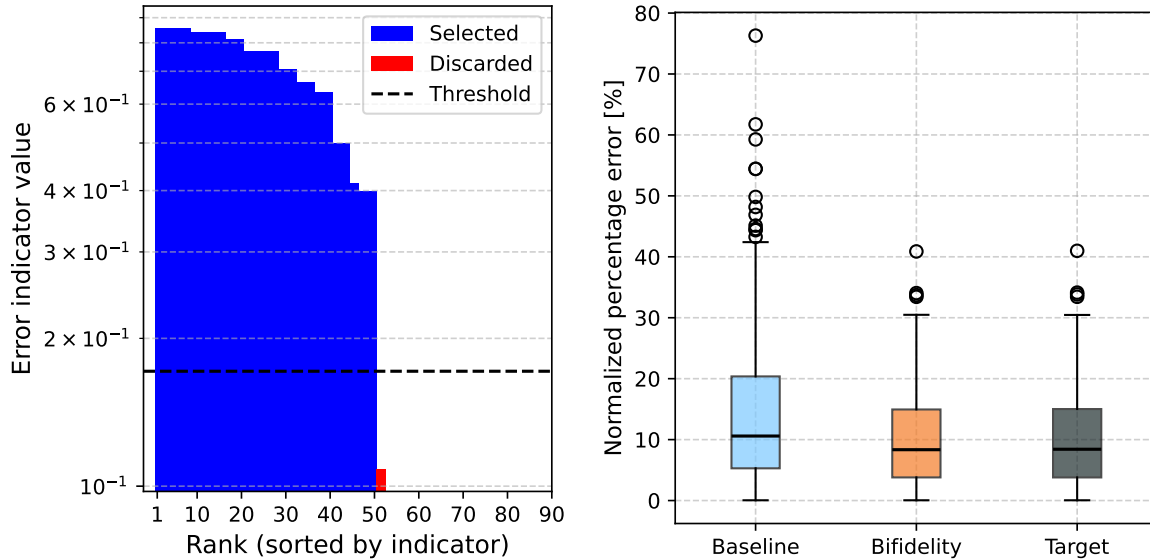


Figure 1: Left: local-error indicator for the Sobol function. Right: boxplots of the normalized percentage errors of the baseline, bifidelity, and target surrogate model of the Sobol function.

where the domain is $\Gamma = [0, 1]^d$. The coefficients a_i are chosen to control the importance of each variable and are set to $a_i = (i - 1)/2$. The function is most sensitive to the first dimensions, testing the ability of our algorithm to correctly allocate refinement points.

Figure 1-left shows the values of the local-error indicator η in Equation 1 for the collocation points in \mathcal{X}_{cand} , sorted decreasingly ($\eta = 0$ after the 50th node, so these values do not appear in this log-scale plot). Applying a threshold criterion with $\tau = 0.2$ in Equation (2), i.e., selecting the candidate points whose indicator exceeds 20% of the maximum indicator value, leads to a set \mathcal{X}_{sel} with 50 points out of 96; if, instead, the elbow selection method had been used, the algorithm would have included 52 points in \mathcal{X}_{sel} . The quality of the resulting bifidelity approximation is shown in Figure 1-right, that reports the boxplots of the normalized percentage error for the bifidelity model $\mathcal{B}[f]$, baseline sparse grid $\mathcal{A}_2[f]$, and the target sparse grid $\mathcal{A}_3[f]$, evaluated at 200 randomly selected test points in Γ . For the bifidelity model $\mathcal{B}[f]$, this error is defined at each test point \mathbf{x}_i as

$$\varepsilon_i = 100 \times \frac{|\mathcal{B}[f](\mathbf{x}_i) - f(\mathbf{x}_i)|}{\max_j f(\mathbf{x}_j) - \min_j f(\mathbf{x}_j)}.$$

which provides a scale-independent metric invariant under affine rescaling of f ; for the baseline and target sparse grids, errors are defined analogously. The baseline model exhibits a broad error distribution, with a large interquartile range and a heavy tail of large errors, reaching up to 80%. Conversely, the bifidelity model displays a sharper concentration around lower errors, with a smaller median, a smaller interquartile range, and a significantly less pronounced tail of large errors: the largest recorded error is indeed approximately half of the largest error of the baseline model, and the number of outlier errors is much smaller. Moreover (and crucially), the performance of the bifidelity model is comparable to that of the target model, showing that the bifidelity strategy can successfully match the accuracy of a more refined surrogate model for a fraction of the computational cost.

Figures 2 and 3 validate visually these results, by comparing the three surrogate models (baseline, bifidelity, and target) against the true Sobol function: the former Figure plots the cross-section on (x_1, x_2) plane, fixing $x_3 = x_4 = 0$, while the latter one shows the cross-section on the line defined by $x_2 = x_3 = x_4 = 0.5$. These figures confirm that the baseline model provides an overall coarse approximation of the overall trend of f . In Figure 2 this surrogate model is somehow acceptable in the center of the domain but completely fails to capture the localized features near the corners of the domain; in Figure 3 the behavior of the baseline is conversely acceptable at the extrema of the domain as well, but the surrogate model is overall too “wobbly”. Conversely, and consistently with Figure 1-right, the target and bifidelity models are nearly identical and reasonably capture both the overall trends and the localized features of the function

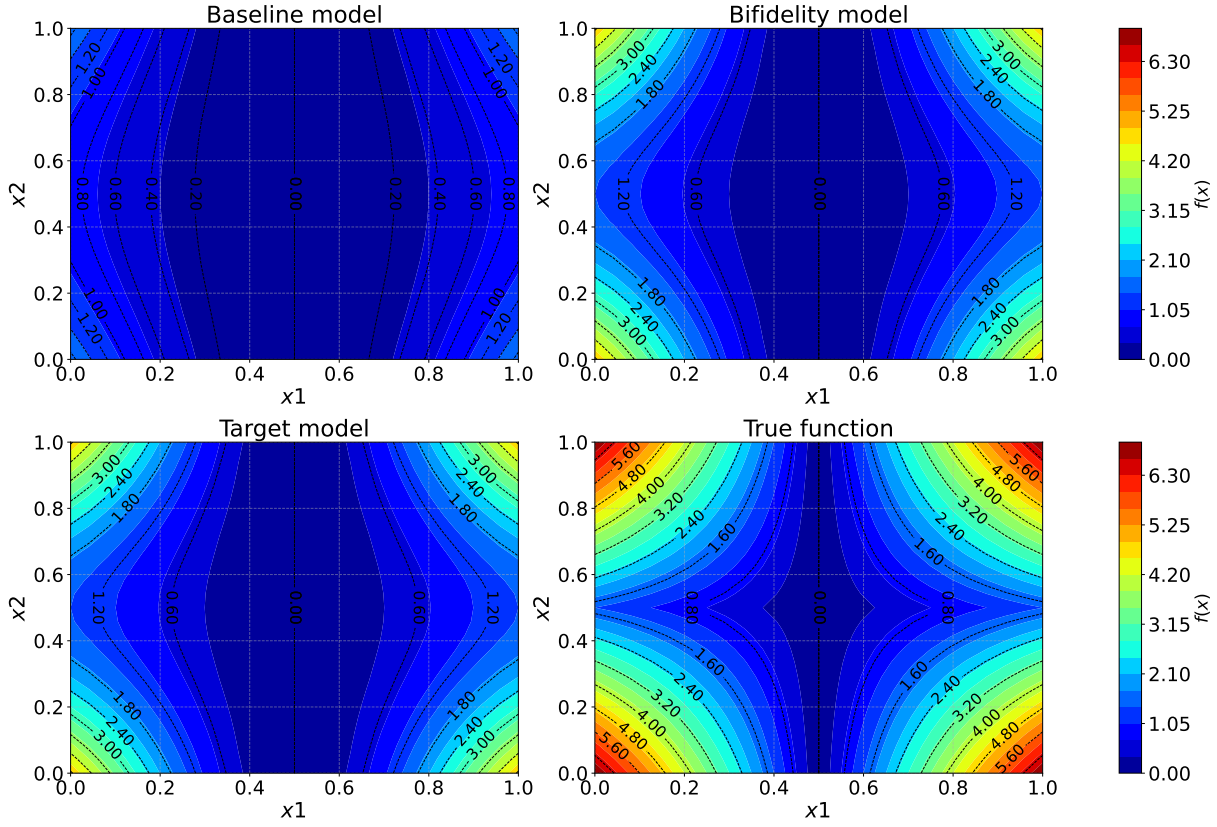


Figure 2: Baseline, bifidelity, and target surrogate models compared against the Sobol function at $x_3 = x_4 = 0$.

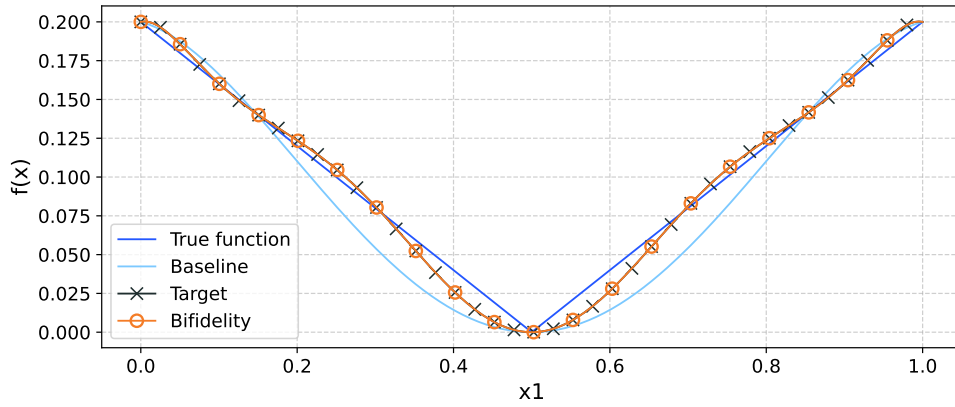


Figure 3: Baseline, bifidelity, and target surrogate models compared against the Sobol function at $x_2 = x_3 = x_4 = 0.5$.

(i.e., its sharp peaks in the corners of the domain). They thus represent a much better approximation of the Sobol function, and, most importantly, this result is reached by the bifidelity approximation with half the cost of the target surrogate model (50 additional evaluations of f rather than 96).

Finally, we discuss the sensitivity to the number of points included in \mathcal{X}_{sel} , i.e., we monitor how the approximation quality evolves as the computational budget increases. In details, we construct a sequence of bifidelity surrogate models, each incorporating an increasing number of refinement points starting from $\mathcal{X}_{sel} = \emptyset$, i.e., the bifidelity model is identical to the baseline sparse grid ($\mathcal{B}[f] = \mathcal{A}_2[f]$), until $\mathcal{X}_{sel} = \mathcal{X}_{cand}$, i.e. the bifidelity model is identical to the target grid ($\mathcal{B}[f] = \mathcal{A}_3[f]$). For each configuration, we then evaluate the maximum absolute error and the Root Mean Square Error (RMSE) with respect to f on a set

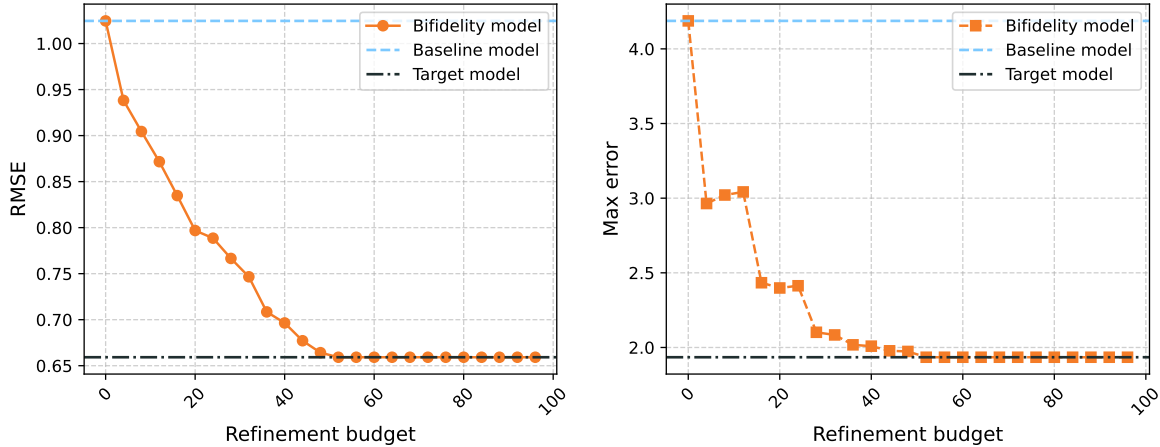


Figure 4: Convergence of RMSE (left) and maximum absolute error (right) for the bifidelity approximation of the Sobol function.

of 200 randomly distributed test points, and report the results in Figure 4. Both the maximum absolute error and the RMSE decrease steadily, indicating a monotonic convergence behavior. As the number of function evaluations grows, we observe a convergence plateau beyond which further point additions result in negligible error reduction. This confirms that in general a bifidelity approach is enough to recover full accuracy of the target sparse grid approximation, i.e., the target sparse grid approximation has in a way some “lossless compressibility” property. The amount of computational savings depends of course on the specific function as well as on the ability of the local-error indicator function to mimic the decay of the actual error, which in this case is pretty good, since it also predicts a decay of the error up to about 50 points.

3.1.2 The Ishigami Function

The Ishigami function [28] is a non-linear, non-monotonic benchmark ($d = 3$), characterized by a strong interaction between its first and third variables. It is defined as:

$$f(\mathbf{x}) = \sin(x_1) + a \sin^2(x_2) + bx_3^4 \sin(x_1),$$

where the input domain is $\mathbf{x} \in [-\pi, \pi]^3$, and the standard coefficients are $a = 7$ and $b = 0.1$. The combination of monotonic and periodic components makes this function a comprehensive test case.

Figure 5-left shows the values of the local-error indicator η for the collocation points in \mathcal{X}_{cand} , sorted decreasingly. Contrary to the previous test, in this case the local-error indicator is equal to one for most of the points, meaning that a ranking of points is not really possible. This is due to the fact that the value of the Ishigami function at the collocation points used to build the coarse model $\mathcal{A}_1[f]$ (7 points) is always zero: therefore, $\mathcal{A}_1[f] = 0$ on the entire domain, and the normalized local error becomes $\eta(\mathbf{x}) = 1$ for most points in \mathcal{X}_{cand} , see Equation (1); the only exceptions are those points at which also $\mathcal{A}_2[f] = 0$ and hence $\eta(\mathbf{x}) = \Delta(\mathbf{x}) = 0$. Including in \mathcal{X}_{sel} all the points with $\eta(\mathbf{x}) = 1$ results in a set \mathcal{X}_{sel} with 36 points out of 44, that are then used to construct the bifidelity surrogate model. Figure 5 (right) presents then the boxplot of the percentage error for the baseline sparse grid $\mathcal{A}_2[f]$, the bifidelity model $\mathcal{B}[f]$, and the target sparse grid $\mathcal{A}_3[f]$ evaluated over 200 randomly selected test locations. The results are qualitatively similar to the previous test: the baseline model exhibits a broad error distribution, with large interquartile range, heavy tails and large errors reaching up to 50%. In contrast, the bifidelity model shows a sharply concentrated distribution around lower error values, with no instances exceeding 10% and overall performance identical to that of the target model, confirming that the bifidelity surrogate model can effectively reproduce the accuracy of a more refined surrogate model at a fraction of the cost.

Figures 6 and 7 compare again the three surrogate models (baseline, bifidelity, and target) against the true Ishigami function. The former Figure plots the cross-section on (x_1, x_2) plane, fixing $x_3 = \pi$, while the latter one plots the cross-section on the line defined by $x_1 = x_3 = \pi$. Like in the case of the Sobol functions, These figures confirm that the baseline model merely provides a coarse approximation of

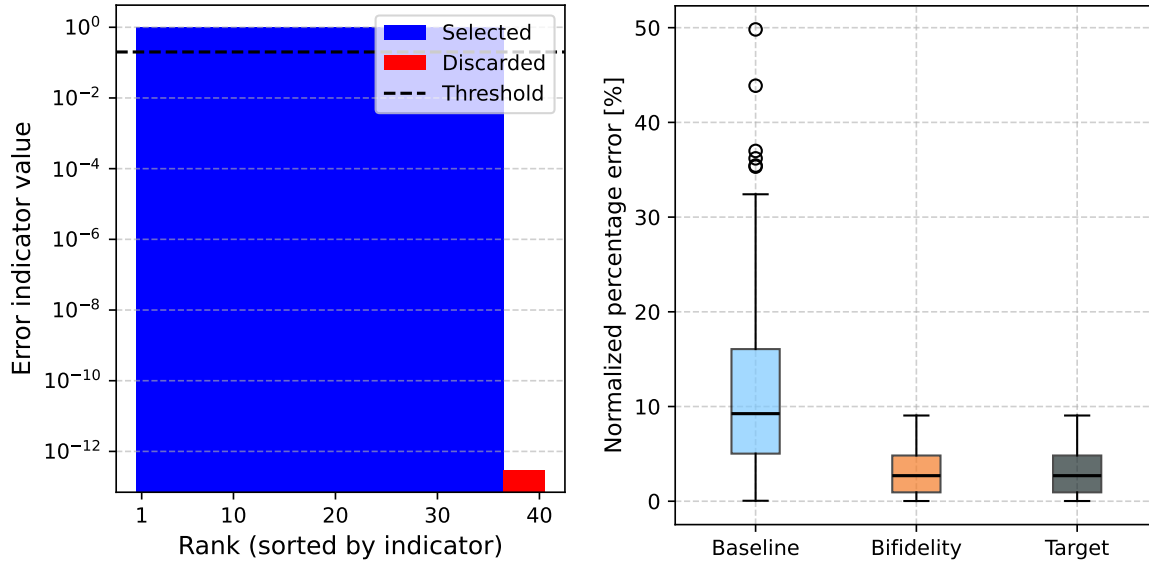


Figure 5: Left: local-error indicator for the Ishigami function. Right: boxplots of the normalized percentage errors of the baseline, bifidelity, and target surrogate model of the Ishigami function.

the overall trend of the Ishigami function. It fails to capture both the location and the amplitude of the sine-induced peaks, resulting in a visibly smeared approximation. Conversely, the target and bifidelity models are nearly identical; moreover, in this case both essentially capture the entire landscape of the Ishigami function. Once again, the bifidelity model reaches the accuracy of the target surrogate model with a smaller computational cost (36 function evaluations instead of 44, corresponding to a sizeable 18% computational saving).

Finally, we discuss also for this test the sensitivity to the number of points in \mathcal{X}_{sel} (see Figure 8). As in the previous case, the errors decrease steadily as the refinement set grows, until a plateau is reached. Although in this case the local-error indicator is a poor estimate of such decay, it is still good enough to capture the saturation of the error decay, and to save us a few functions evaluations.

3.1.3 Oscillatory function

In this test we consider an oscillatory function, which provides a smooth, periodic benchmark designed to evaluate the sensitivity of our strategy to heterogeneous frequency content across input dimensions. In our study, we consider a $d = 4$ dimensional function defined as:

$$f(\mathbf{x}) = \sum_{i=1}^d \cos(\theta_i x_i)$$

where the domain is $\mathbf{x} \in [0, 1]^d$. The frequency coefficients θ_i are chosen to induce anisotropic oscillatory behavior: $\boldsymbol{\theta} = [1.5\pi, 3.0\pi, 0.5\pi, 4.5\pi]$. This configuration results in higher-frequency oscillations along x_2 and x_4 , and lower-frequency variation along x_3 , introducing directional gradients of different intensity. The function is continuously differentiable and free of discontinuities, making it suitable for testing surrogate modeling techniques and adaptive sampling strategies in smooth regimes. Its varying frequency content challenges algorithms to resolve fine-scale features selectively across dimensions.

Figure 9-left illustrates the behavior of the local error indicator for points in \mathcal{X}_{cand} . Applying the threshold-based selection criterion with a cutoff value of 5% results in the selection of $\mathcal{X}_{sel} = 26$ points out of 96. Figure 9 (right) shows the boxplots of the percentage errors for the baseline, target, and bifidelity models. Once again, the baseline model exhibits a broader error distribution, with several points reaching relatively large errors. In contrast, the bifidelity model shows a much more concentrated distribution, maintaining error levels below 10% at all evaluated points, and the target model performs only marginally better.

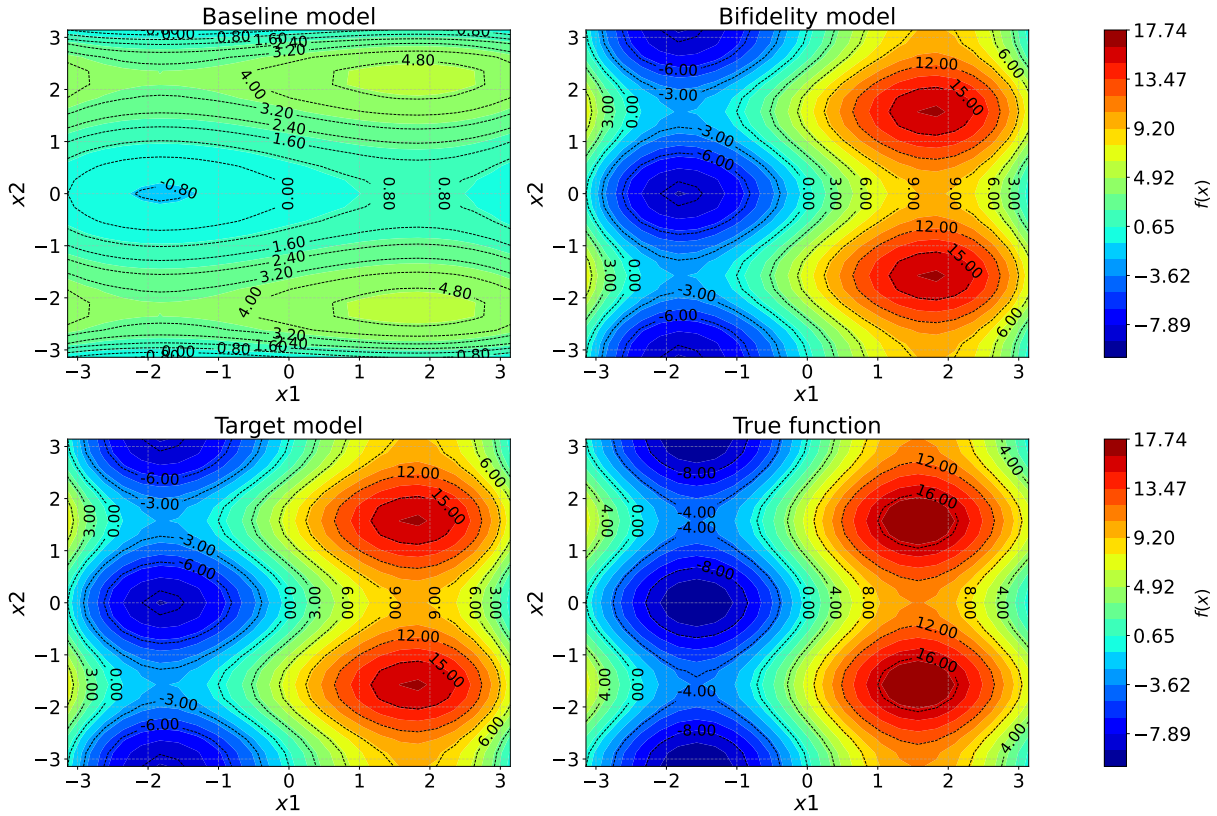


Figure 6: Baseline, bifidelity, and target surrogate models compared against the Ishigami function at $x_3 = \pi$.

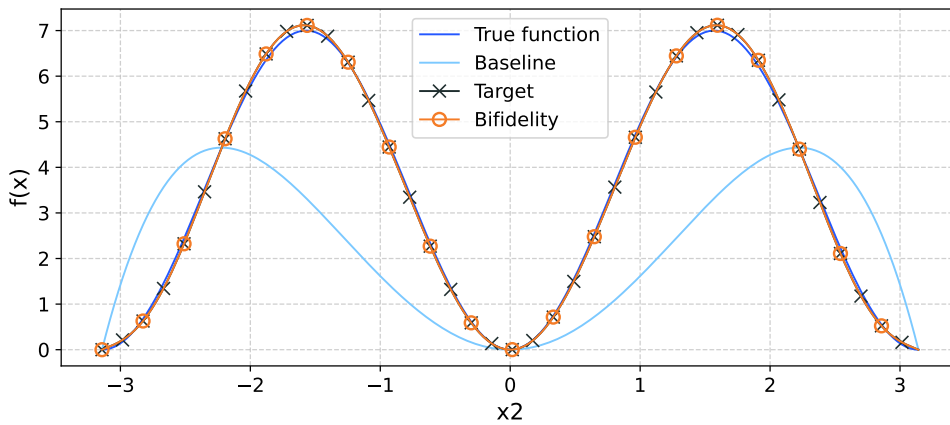


Figure 7: Baseline, bifidelity, and target surrogate models compared against the Ishigami function at $x_1 = x_3 = \pi$

Once more, we compare the three surrogate models (baseline, bifidelity, and target) against the true oscillatory function both in a two-dimensional cross-section (Figures 10, fixing $x_3 = x_4 = 0$), as well as in a one-dimensional cross-section (Figure 11, fixing $x_1 = x_2 = x_3 = 0.5$). Also in this case, it is visually confirmed that the baseline model provides nothing more than a coarse approximation of true function. The 1d-section in Figure 11 shows in particular that even the number of peaks is not properly captured. Conversely, the target and bifidelity models provide a very reasonable approximation of the true function and are again nearly identical, which is particularly remarkable since, in this test, the bifidelity surrogate uses only about a quarter of the function evaluations of the target surrogate (26 out of 96).

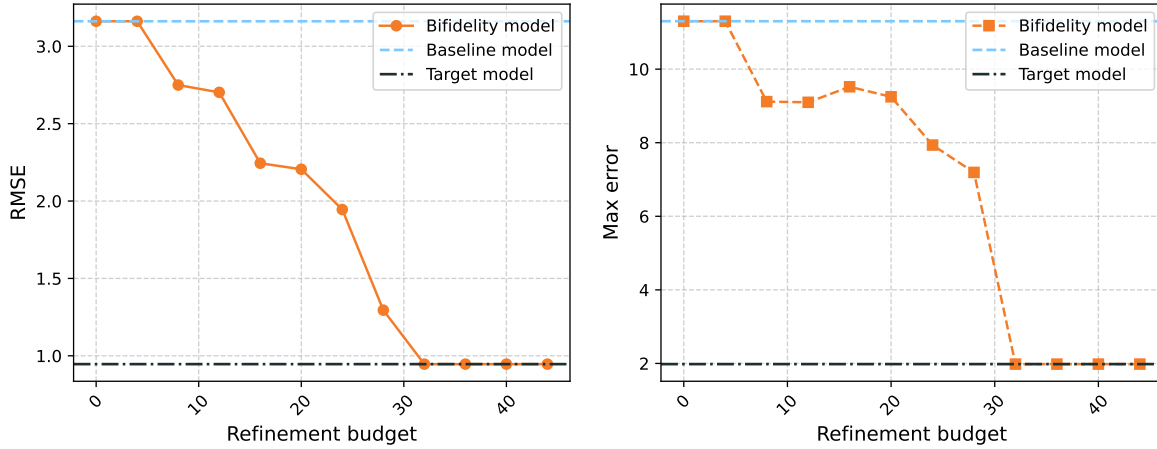


Figure 8: Convergence of RMSE (left) and maximum absolute error (right) for the Ishigami’s function.

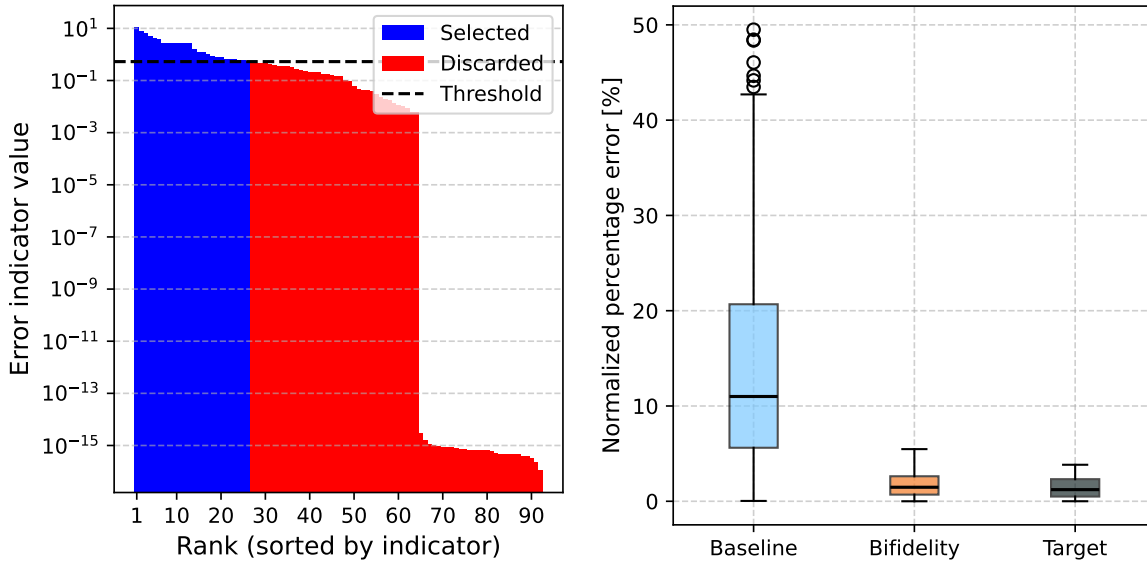


Figure 9: Left: local-error indicator for the oscillatory function. Right: boxplots of the normalized percentage errors of the baseline, bifidelity, and target surrogate model of the oscillatory function.

Finally, as for the previous benchmarks, Figure 12 illustrates the sensitivity to the number of points in \mathcal{X}_{sel} . Also in this case, the plot shows a progressive reduction in both the maximum absolute error and the RMSE, that sharply drop to a plateau after only 26 refinement points out of 96 are added. In this case the error indicator is a conservative estimate of the true error (cf. Figure 9-left), that can nonetheless provide a helpful guidance in reducing the computational cost: in the worst-case scenario in which \mathcal{X}_{sel} had included all points where η is not numerically zero (around 65 points), it would have still signified a saving of around 30 points to reach full accuracy, i.e. a saving of around 30% with respect to the target model.

3.2 Application to the hydrogen-fueled perforated burners case study

The primary objective of the proposed bifidelity methodology is to enable efficient and accurate surrogate modeling of complex engineering systems, for which direct evaluations of the full numerical model are computationally expensive. To demonstrate its practical applicability, we consider a representative case study concerning the design of a hydrogen-fueled perforated burner. In such systems, flashback phenomena pose critical risks due to hydrogen’s high flame speed and diffusivity: it is therefore essential to systematically

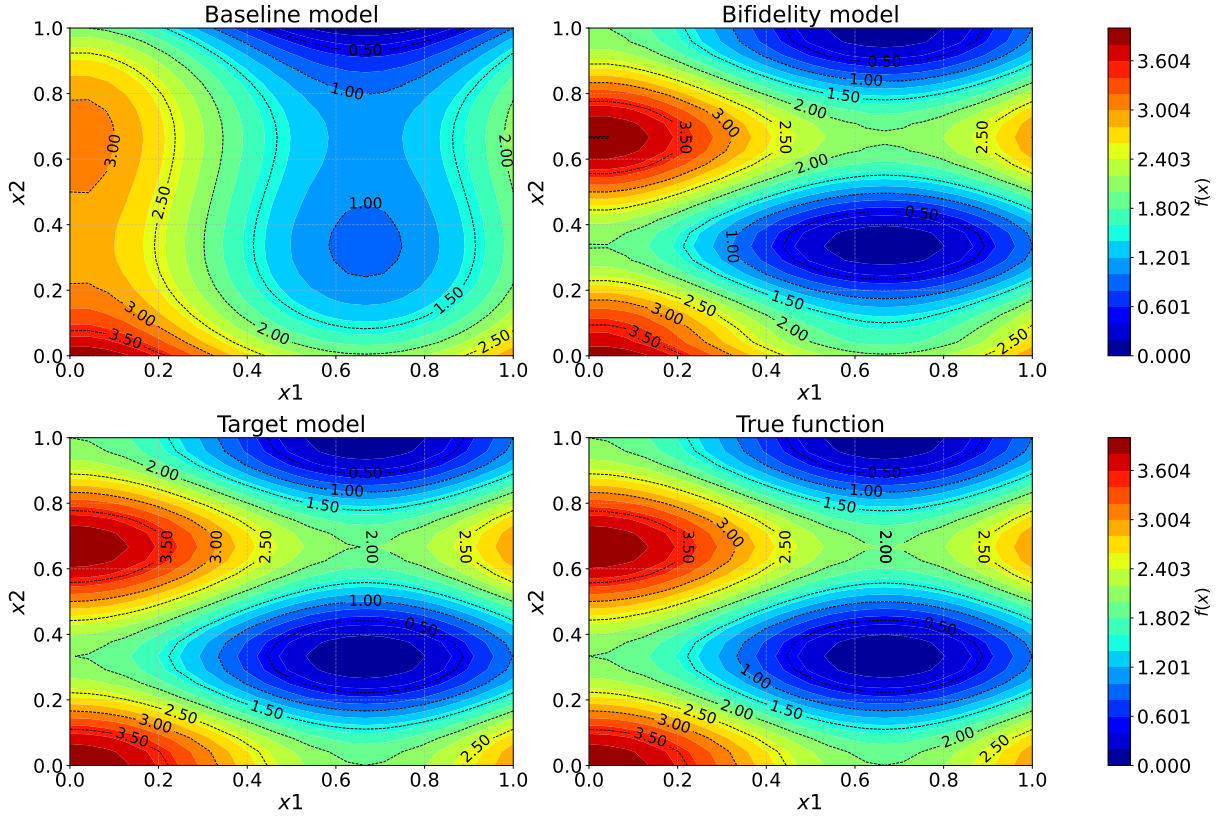


Figure 10: Baseline, bifidelity, and target surrogate models compared against the oscillatory function at $x_3 = x_4 = 0$

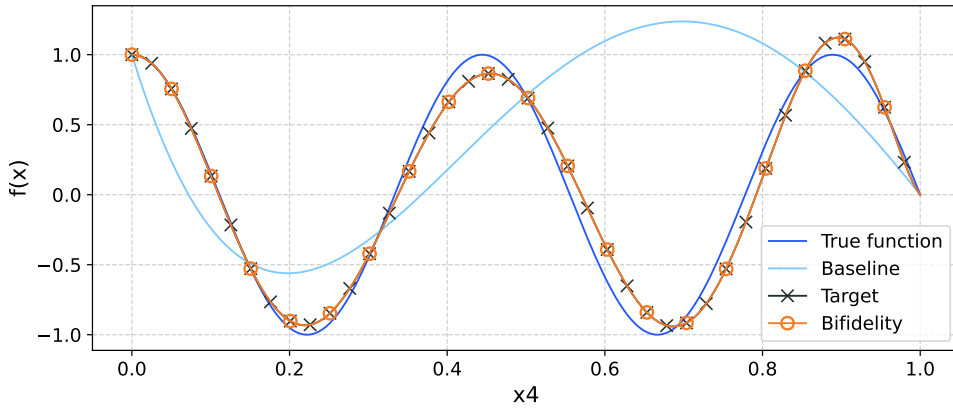


Figure 11: Baseline, bifidelity, and target surrogate models compared against the oscillatory function at $x_1 = x_2 = x_3 = 0.5$.

assess how the flashback behavior is influenced by the geometry of the burner, to optimize the design of such devices while guaranteeing safety and control strategies, as well as to select configurations of experimental interest (see also [30] for a related sensitivity analysis study). With these objectives in mind, our goal here is to derive a surrogate model of the flashback velocity as a function of the geometrical design parameters of the burner.

In detail, we consider a three-dimensional segment of a perforated stainless steel burner plate with a single slit, parameterized by four geometric variables: slit length (L), slit width (W), inter-slit spacing (D), and plate thickness (H), as shown in Figure 13. The parameters vary within the following ranges: $L \in [0, 4]$ mm, $W \in [0.4, 0.8]$ mm, $D \in [0.3, 1.7]$ mm, and $H \in [0.3, 0.9]$ mm. In this computational domain,

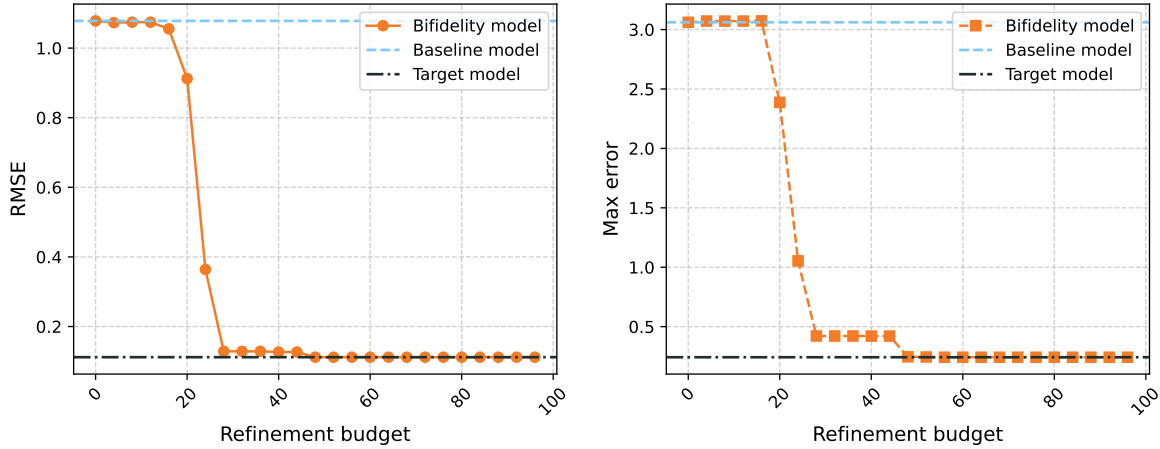


Figure 12: Convergence of RMSE (left) and maximum absolute error (right) for the oscillatory function.

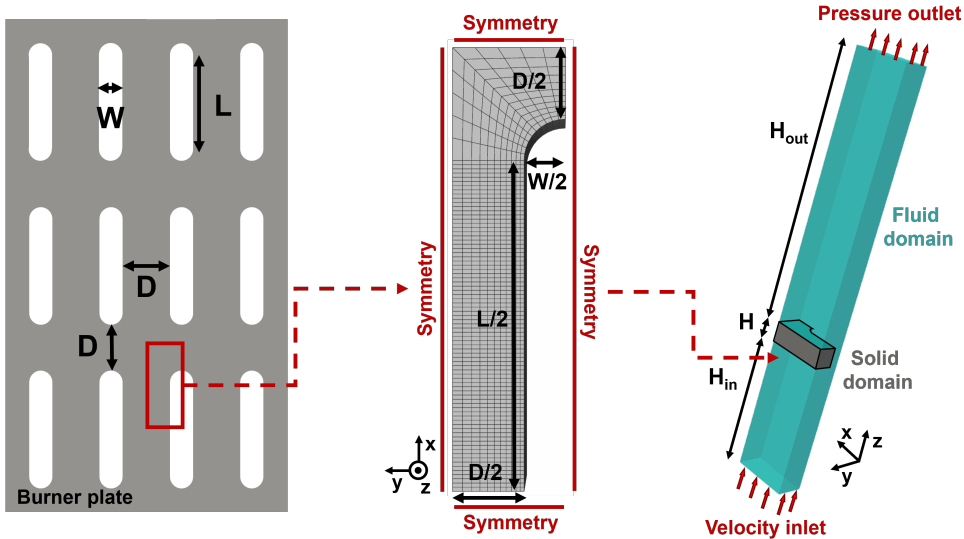


Figure 13: Left panel: Slit pattern on the burner plate, highlighting the section of the computational domain. Center panel: Slit geometry (boundary conditions in red) and solid plate mesh. Right panel: Computational domain (fluid zone in light blue, solid zone in gray, boundary conditions in red). Reproduced from [35].

we consider the flow of a mixture of air and hydrogen, modeled by steady, laminar, compressible Navier–Stokes equations, coupled with diffusion-transport-reaction equations for the chemical species, together with an ideal-gas equation of state. The simulations consider a hydrogen–air mixture at equivalence ratio $\phi = 0.6$, with uniform inlet conditions ($T_u = 300$ K) and an ambient pressure outlet ($p = 1$ atm). For all cases investigated, the Reynolds number of the resulting jet remains within the laminar regime and no turbulence modeling is employed. Thermal coupling between the fluid and solid domains is enforced through a conjugate heat transfer formulation, while chemical kinetics are described using a reduced mechanism comprising 9 species and 22 reactions [31].

The governing equations are discretized on a structured three-dimensional mesh with local refinement in the reaction region. The characteristic cell size in the flame zone is approximately $\Delta x \simeq 25 \mu\text{m}$, corresponding to about $\delta_F/13$, where δ_F denotes the unstretched one-dimensional thermal flame thickness. Depending on the geometric configuration, the total number of control volumes ranges from approximately 3×10^5 to 3×10^6 . This resolution was selected based on grid-independence analyses reported in previous studies [32, 33, 34, 35]. All simulations are performed using *ANSYS Fluent 24.2*.

The critical flashback condition is determined through a sequence of steady reacting-flow simulations.

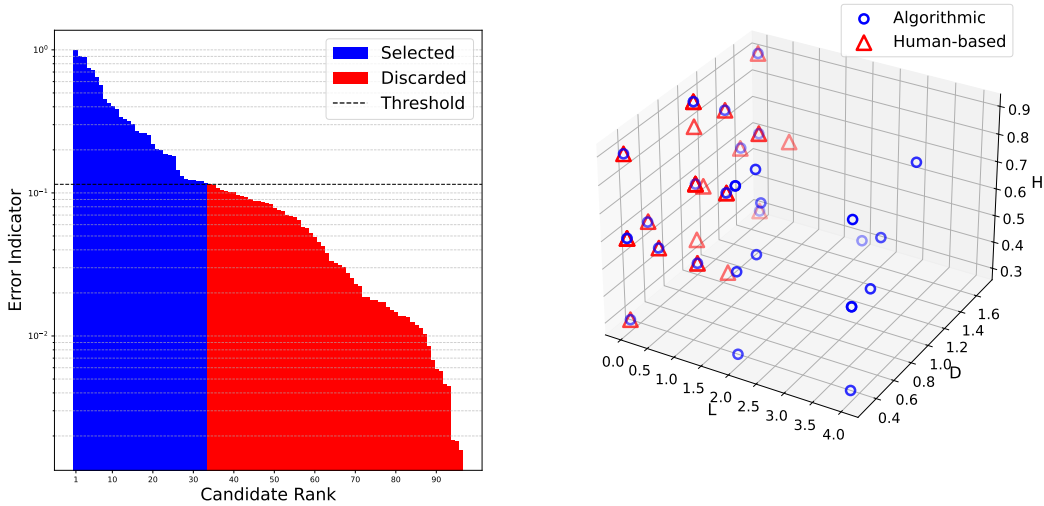


Figure 14: Local error indicator for collocation points in \mathcal{X}_{cand} for the burner problem, sorted decreasingly (left) and \mathcal{X}_{sel} for the human-based and algorithmic strategies (right)

For a given burner geometry, a stable flame solution is first established at a sufficiently high inlet velocity, ensuring that flashback does not occur. The inlet velocity is then progressively reduced, and successive steady-state simulations are performed until the solver can no longer converge to a stable flame solution. This loss of convergence is interpreted as the onset of flashback. The corresponding critical flashback velocity is defined as the cold-flow bulk velocity at the slit entry,

$$V_{FB} = \frac{A_{tot}}{A_{slit}} V_{in} = \frac{V_{in}}{\psi},$$

where V_{in} is the imposed inlet velocity and $\psi = A_{slit}/A_{tot}$ denotes the burner porosity. This definition provides an intrinsic measure of the configuration resistance to flashback, independent of trivial geometric scaling. Further details on the numerical procedure and its validation are reported in [32, 33, 34, 35]. Each evaluation of V_{FB} thus requires multiple fully coupled three-dimensional reacting-flow simulations with detailed chemistry and conjugate heat transfer. As a result, a single high-fidelity evaluation typically entails wall-clock times of several days up to approximately one week on $\mathcal{O}(10^2)$ parallel processors. This computational burden renders exhaustive sampling of the parametric space impractical and provides the primary motivation for the (bifidelity) surrogate modeling strategy introduced in this work.

In a previous study [30] an earlier version of the bifidelity strategy described in the current work was proposed to refine the baseline surrogate model (obtained also in this case for $w = 2$) in the region $L \approx 0$ of the parametric space; specifically, the chosen set \mathcal{X}_{sel} consisted of 33 points. Crucially however, this decision was guided by expert judgement, based on prior experience and knowledge/physical intuition about the problem at hand; in the following, we refer to this construction as “human-based bifidelity approach”. In the current study, we aim instead at making the bifidelity strategy entirely algorithmic instead (in the following, “algorithmic bifidelity approach”), by introducing the local error indicator η and the construction strategy in Equation (3).

The two scalar output quantities of interest are flashback velocity and maximum burner temperature. Thus, the refinement process can be guided by either quantity. We observed that the resulting performance exhibits no significant differences depending on the variable chosen to drive the refinement, so in what follows, we refer to the process using the flashback velocity as the guiding quantity. Figure 14 (left) presents the local error indicator computed for the points in \mathcal{X}_{cand} , ranked in decreasing order of importance: to allow a fair comparison between the human-based approach from [30] and the automatic bifidelity strategy, the budget in this study was fixed at 33 points. The sets \mathcal{X}_{sel} selected by the human-based and the algorithmic approaches are then shown in Figure 14 (right), in the three-dimensional (L, D, H) space at $W = 0.6$ mm. While the two sets are not identical, the bifidelity model successfully recovers the majority of the points identified by the human-based approach, particularly in regions where the function

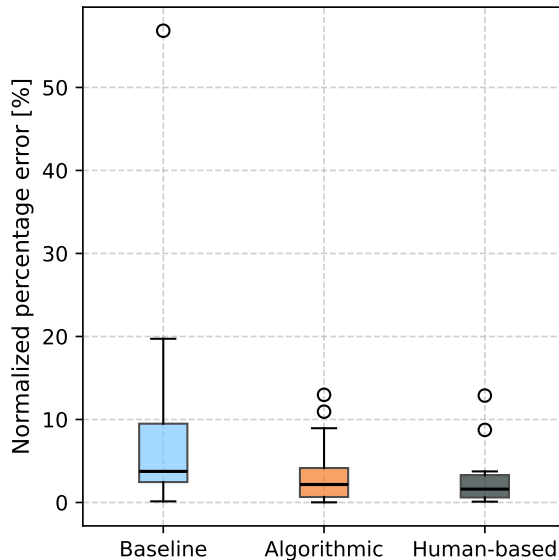


Figure 15: Boxplots of the normalized percentage error for the baseline, human-based and the algorithmic bifidelity surrogate model for the flashback velocity

exhibits strong gradients or localized features. This overlap confirms the effectiveness of the local-error indicator in targeting the most informative regions of the domain. In addition to this basic agreement, the bifidelity strategy introduces a few supplementary points in more peripheral or less active areas of the input space. Overall, the comparison highlights the capacity of the algorithmic strategy to emulate expert-driven refinement while offering a more systematic and scalable alternative.

Figure 15 shows the boxplots of the normalized percentage error for three models: the baseline model, the human-based bifidelity approach, and the algorithmic bifidelity approach. Since no analytical reference values are available in this experimental setting, the comparison is performed against 17 additional simulations, taken at locations as far as possible from the collocations points used to build the surrogate models. This ensures an unbiased evaluation of each model’s generalization capability. The results clearly demonstrate that the algorithmic approach achieves a substantial improvement over the baseline model and confirms its effectiveness in capturing the underlying physical behavior with minimal computational cost. Importantly, it also achieves error distributions closely aligned with those of the human-based approach. The small difference should be weighted against the fact that such expert-driven refinement is feasible only when deep physical insight and domain-specific experience are available. By contrast, the algorithmic strategy requires no prior knowledge and is fully automated, making its near-expert performance particularly valuable and naturally scalable.

Finally, Figure 16 compares the response surfaces for flame velocity for baseline model, the human-based bifidelity model, and the algorithmic-based bifidelity model. As expected from the error boxplots, the human-based and algorithmic bifidelity models produce nearly identical predictions, exhibiting a sharper representation of the velocity gradient across the domain, especially in regions where the baseline model tends to oversmooth the underlying physical behavior.

4 Conclusions

In this work, we introduce a novel bifidelity framework for constructing sparse-grid surrogate models as an alternative to traditional adaptive methods, which can lead to significant computational savings. The core of our contribution is a zero-cost error indicator that leverages on two nested, pre-existing surrogates to obtain an efficient a priori ranking of candidate points where the expensive function can be evaluated. This allows a surrogate model construction in which the computational budget is allocated exclusively to the most impactful regions of the parameter space.

The effectiveness of the proposed methodology was validated through a series of numerical investigations. First, its robustness and efficacy was demonstrated on a set of analytical benchmark functions.

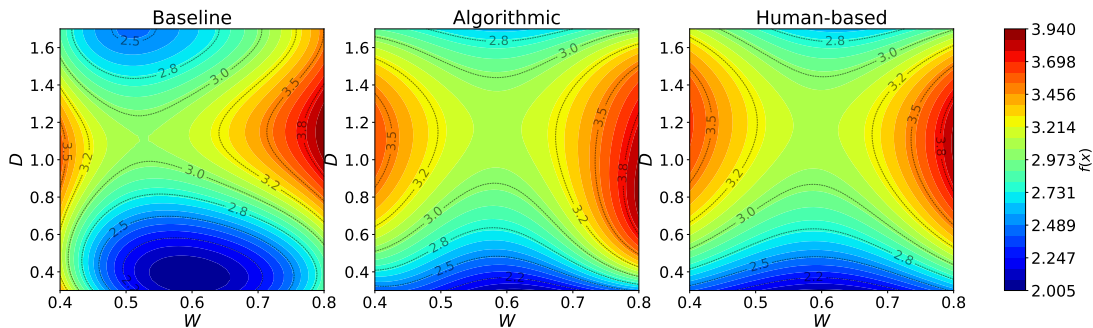


Figure 16: Comparison of the surrogate models for the flashback velocity in our case study at $L = 0.0$ and $H = 0.6$

The results consistently showed that our bifidelity model achieves an accuracy closely approaching that of a target sparse grid surrogate model, while requiring only a fraction of the computational budget. This confirms that the proposed zero-cost indicator is highly effective at identifying the most salient points for grid refinement.

The practical applicability of the framework was then demonstrated on a computational dataset from a hydrogen-fueled perforated burner problem. In this real-world scenario, our method yielded excellent results, comparable to those obtained from a specialized, human-based refinement of the surrogate model. A remarkable finding was that our algorithm automatically identified the majority of the refinement points that had been manually selected in the human-based approach based on specific knowledge.

Future work will focus on applying this framework to a broader range of complex engineering problems, particularly in the context of optimization and uncertainty quantification. Further research could also explore the formulation of more sophisticated error indicators and the integration of this adaptive strategy within multi-fidelity modeling workflows.

Acknowledgments This work has been supported by the ICSC-Centro Nazionale di Ricerca in High Performance Computing, Big Data, and Quantum Computing, both funded by European Union - NextGenerationEU. Lorenzo Tamellini has been partially supported by the project 202222PACR “Numerical approximation of uncertainty quantification problems for PDEs by multi-fidelity methods (UQ-FLY)” and is member of the Gruppo Nazionale Calcolo Scientifico-Istituto Nazionale di Alta Matematica (GNCS-INdAM).

Data Availability Statement The Python toolbox developed for the algorithmic bifidelity approach is open-source and available at <https://github.com/cfdlab-unipi/surrogate-informed-sparse-grid-tool>. It is released under the MIT license, allowing unrestricted use, modification, and redistribution. The toolbox implements in Python some of the basic functionalities of the Sparse Grid Matlab Kit [24] and extends it by incorporating the algorithmic bifidelity logic introduced in this work, providing a fully Python-based framework for surrogate construction and analysis. It supports scalar outputs, time-series data, and vector-valued quantities. All scripts required to reproduce the figures and results presented in this work are included in the repository.

Credit Statement **Matteo Rosellini:** Conceptualization, implementation and data curation, Writing - first draft; **Filippo Fruzza:** Conceptualization, implementation and data curation, Writing - first draft; **Alessandro Mariotti:** Methodology, Writing – review & editing. **Maria Vittoria Salvetti:** Methodology, Conceptualization, Writing – review & editing. **Lorenzo Tamellini:** Methodology, Conceptualization, Writing – review & editing.

References

- [1] R. Ghanem, D. Higdon, and H. Owhadi. *Handbook of Uncertainty Quantification*. Springer, Cham, 2016.

- [2] H.-J. Bungartz and M. Griebel. Sparse grids. *Acta Numerica*, 13:147–269, 2004.
- [3] I. Babuška, F. Nobile, and R. Tempone. A stochastic collocation method for elliptic partial differential equations with random input data. *SIAM Review*, 52(2):317–355, June 2010.
- [4] D. Xiu and J.-S. Hesthaven. High-order collocation methods for differential equations with random inputs. *SIAM Journal on Scientific Computing*, 27(3):1118–1139, 2005.
- [5] R. E. Bellman. *Adaptive Control Processes: A Guided Tour*. Princeton University Press, Princeton, NJ, 1961.
- [6] A. Chkifa, A. Cohen, R. DeVore, and C. Schwab. Sparse adaptive Taylor approximation algorithms for parametric and stochastic elliptic PDEs. *ESAIM: Mathematical Modelling and Numerical Analysis*, 47(1):253–280, 2013.
- [7] J. Beck, F. Nobile, L. Tamellini, and R. Tempone. On the optimal polynomial approximation of stochastic PDEs by Galerkin and collocation methods. *Mathematical Models and Methods in Applied Sciences*, 22(09), 2012.
- [8] M. Eigel, O. G. Ernst, B. Sprungk, and L. Tamellini. On the convergence of adaptive stochastic collocation for elliptic partial differential equations with affine diffusion. *SIAM Journal on Numerical Analysis*, 60(2):659–687, 2022.
- [9] M. Feischl and A. Scaglioni. Convergence of adaptive stochastic collocation with finite elements. *Computers & Mathematics with Applications*, 98:139–156, 2021.
- [10] M. Obersteiner and H.-J. Bungartz. A generalized spatially adaptive sparse grid combination technique with dimension-wise refinement. *SIAM Journal on Scientific Computing*, 43(4):A2381–A2403, 2021.
- [11] X. Ma and N. Zabarar. An adaptive hierarchical sparse grid collocation algorithm for the solution of stochastic differential equations. *Journal of Computational Physics*, 228(8):3084–3113, 2009.
- [12] M. F. Rehme, F. Franzelin, and D. Pflüger. B-splines on sparse grids for surrogates in uncertainty quantification. *Reliability Engineering & System Safety*, 209:107430, 2021.
- [13] A. Eftekhari and S. Scheidegger. High-dimensional dynamic stochastic model representation. *SIAM Journal on Scientific Computing*, 44(3):C210–C236, 2022.
- [14] D. Pflüger, B. Peherstorfer, and H.-J. Bungartz. Spatially adaptive sparse grids for high-dimensional data-driven problems. *Journal of Complexity*, 26(5):508–522, 2010. SI: HDA 2009.
- [15] J. D. Jakeman, R. Archibald, and D. Xiu. Characterization of discontinuities in high-dimensional stochastic problems on adaptive sparse grids. *Journal of Computational Physics*, 230(10), 2011.
- [16] H. R. Fairbanks, L. Jofre, G. Geraci, G. Iaccarino, and A. Doostan. Bi-fidelity approximation for uncertainty quantification and sensitivity analysis of irradiated particle-laden turbulence. *Journal of Computational Physics*, 402:108996, 2020.
- [17] J. Hampton, H. R. Fairbanks, A. Narayan, and A. Doostan. Practical error bounds for a non-intrusive bi-fidelity approach to parametric/stochastic model reduction. *Journal of Computational Physics*, 368:315–332, 2018.
- [18] J. A. Christen and C. Fox. Markov chain monte carlo using an approximation. *Journal of Computational and Graphical Statistics*, 14(4):795–810, 2005.
- [19] E. Laloy, B. Rogiers, J. A. Vrugt, D. Mallants, and D. Jacques. Efficient posterior exploration of a high-dimensional groundwater model from two-stage markov chain monte carlo simulation and polynomial chaos expansion. *Water Resources Research*, 49(5):2664–2682, 2013.
- [20] A. Manzoni, S. Pagani, and T. Lassila. Accurate solution of bayesian inverse uncertainty quantification problems combining reduced basis methods and reduction error models. *SIAM/ASA Journal on Uncertainty Quantification*, 4(1):380–412, 2016.

- [21] S. Pagani, A. Manzoni, and A. Quarteroni. Efficient state/parameter estimation in nonlinear unsteady PDEs by a reduced basis ensemble kalman filter. *SIAM/ASA Journal on Uncertainty Quantification*, 5(1):890–921, 2017.
- [22] C. H. Choi, A. Zaroni, A. L. Marsden, and D. Schiavazzi. On the performance of multi-fidelity and reduced-dimensional neural emulators for inference of physiological boundary conditions. *Computers in Biology and Medicine*, 200:111389, 2026.
- [23] F. Nobile, L. Tamellini, F. Tesei, and R. Tempone. An adaptive sparse grid algorithm for elliptic PDEs with lognormal diffusion coefficient. In J. Garcke and D. Pflüger, editors, *Sparse Grids and Applications — Stuttgart 2014*, volume 109 of *Lecture Notes in Computational Science and Engineering*, pages 191–220. Springer, Cham, 2016.
- [24] C. Piazzola and L. Tamellini. Algorithm 1040: The sparse grids matlab kit—a matlab implementation of sparse grids for high-dimensional function approximation and uncertainty quantification. *ACM Transactions on Mathematical Software*, 50(1):1–22, 2024.
- [25] A. M. Stuart. Inverse problems: A bayesian perspective. *Acta Numerica*, 19:451–559, 2010.
- [26] T. Gerstner and M. Griebel. Dimension–adaptive tensor–product quadrature. *Computing*, 71(1):65–87, 2003.
- [27] Il’ya Meerovich Sobol’. On sensitivity estimation for nonlinear mathematical models. *Matematicheskoe modelirovanie*, 2(1):112–118, 1990.
- [28] T. Ishigami and T. Homma. An importance quantification technique in uncertainty analysis for computer models. In *Proceedings of the First International Symposium on Uncertainty Modeling and Analysis*, pages 398–403. IEEE, 1990.
- [29] A. Saltelli, P. Annoni, I. Azzini, F. Campolongo, M. Ratto, and S. Tarantola. Variance based sensitivity analysis of model output. design and estimator for the total sensitivity index. *Computer Physics Communications*, 181(2):259–270, 2010.
- [30] F. Fruzza, R. Lamioni, T. Grenga, A. Mariotti, M. V. Salvetti, and C. Galletti. Mapping flashback velocity in hydrogen-fueled perforated burners over a broad geometric design space. *International Journal of Hydrogen Energy*, 202:152980, 2026.
- [31] R. W. Bilger, S. H. Stårner, and R. J. Kee. On reduced mechanisms for methane-air combustion in non-premixed flames. *Combustion and Flame*, 80:135–149, 1990.
- [32] F. Fruzza, R. Lamioni, L. Tognotti, and C. Galletti. Flashback of H₂-enriched premixed flames in perforated burners: Numerical prediction of critical velocity. *International Journal of Hydrogen Energy*, 48:31790–31801, 2023.
- [33] F. Fruzza, R. Lamioni, A. Mariotti, M. V. Salvetti, and C. Galletti. Flashback propensity due to hydrogen blending in natural gas: Sensitivity to operating and geometrical parameters. *Fuel*, 362:130838, 2024.
- [34] F. Fruzza, H. Chu, R. Lamioni, T. Grenga, C. Galletti, and H. Pitsch. The importance of Soret effect, preferential diffusion, and conjugate heat transfer for flashback limits of hydrogen-fueled perforated burners. *Proceedings of the Combustion Institute*, 40(1):105581, 2024.
- [35] F. Fruzza, H. Chu, R. Lamioni, T. Grenga, C. Galletti, and H. Pitsch. Three-dimensional numerical investigation of flashback in premixed hydrogen flames within perforated burners. *Combustion and Flame*, 274:113987, 2025.